GMRT Technical Memo: Constraining Direction-Dependent Instrumental Polarisation

J. S. Farnes*

3rd May, 2012

Abstract

Direction-dependent instrumental polarisation introduces wide-field polarimetric aberrations and limits the dynamic range of low-frequency interferometric images. This restricts the region of the primary-beam usable for scientific measurement. The wide-field beam at the GMRT has been constrained by observations in full-Stokes at 325 MHz and 610 MHz, and found to be essentially frequency-independent across an observing band. The directional dependence is largely independent of the feed and is dominated by the curvature of the dishes reflecting mesh, causing the 325 MHz and 610 MHz polarisation beams to scale with the Stokes *I* FWHM. This direction-dependent polarisation averages down considerably for observations with a large range in parallactic angle. I use the developed beam model to reduce direction-dependent effects in 610 MHz *uv*-data. An analysis of the Stokes *I* beam at 610 MHz suggests the beam has a 'squircle' shaped geometry, potentially affecting the dynamic range obtainable at the GMRT. Furthermore, I also develop a new technique for polarisation angle calibration using the wide-field response of the GMRT. This technique has the advantage that it calibrates the polarisation angle independently of ionospheric variation and source variability. It also removes the need for known polarised sources on the sky – which are scarce at low frequencies.

1 Introduction

Polarised radio emission is fundamentally related to the presence of magnetic fields, and observations of the polarisation properties of non-thermal radio emission are arguably the best way of studying quasi-regular fields and their structure. Polarimetric observations have recently become available at the Giant Metrewave Radio Telescope (GMRT). It is important to be able to complete a polarisation calibration that reliably removes instrumental effects, so that the GMRT's polarisation mode may be used for scientific purposes.

There are two essential steps in the initial polarisation calibration for an alt-az mounted interferometer with circular feeds:

1. Firstly, the orthogonal polarisations of antenna feeds are never perfectly isolated, and corrections must be made for this polarisation 'leakage' between *R* and

*j.farnes@mrao.cam.ac.uk

L. This is typically carried out by observing an unresolved point source at the phase-centre over a range of parallactic angles, allowing for the separation of instrumental and source polarisation.

2. When solving for the instrumental leakage, the absolute value of the phase offset between *R* and *L* is left as an unconstrained degree of freedom. This needs to be corrected by observing a source of known electric vector polarisation angle (EVPA). The calibrators 3C138 and 3C286 are generally used for this purpose.

These two steps provide an 'on-axis' polarisation calibration, and reduce residual instrumental polarisation to a minimum at the phase-centre. This calibration can take significant computing time at the GMRT as the leakages vary rapidly across the band, so the calibration must be carried out on each spectral channel individually.

Any spurious instrumental polarisation results in leakage from Stokes *I* into the *Q* and *U* images. Following on-axis calibration at the GMRT, a residual instrumental polarisation of $\sim 0.5\%$ can typically be obtained at the phase-centre (Farnes 2012).

However, the response of an interferometer varies across the primary beam, and wide-field polarimetry requires calibration of these 'direction-dependent' or 'off-axis' instrumental effects. Similar to the case of on-axis calibration, the 'polarisation beam' manifests itself with flux in total intensity leaking into the polarisation images.

These polarimetric aberrations result in an increase in the observed fractional polarisation and also alter the absolute EVPA of sources – with the effect becoming more pronounced with increasing distance from the phase-centre. Direction-dependent effects therefore limit the dynamic range of low-frequency interferometric images – restricting the region of the primary beam that is useful for scientific measurement.

Following Heiles (1999), there are two kinds of beam polarisation that are theoretically expected:

1. Beam squint: this occurs when the two circular polarisations point in different directions by a certain angle. Beam squint tends to produce a 'two-lobed' pattern, one positive and one negative.

2. Beam squash: this occurs when the two linear polarisations have different beamwidths by a certain amount. Beam squash tends to produce a 'four-lobed' pattern, in which two lobes on opposite sides of the beam centre have the same sign and two lobes rotated by 90° have the opposite sign. This quadrupolar pattern tends to give rise to instrumental linear polarisation that is oriented radially with respect to the phase-centre.

Knowledge of the pattern of beam squint and beam squash across the FOV, and the ability to correct for the resulting direction-dependent effects, is vital for mosaiced surveys and other observations where the science relies on wide-field polarimetric capabilities.

In this memo, an observational analysis of the GMRT beam is provided in full-polarisation at both 325 MHz and 610 MHz. The obtained polarisation beam model is then used to correct for the effects of direction-dependent instrumental polarisation at 610 MHz. Details of the holography observations used to obtain the beam constraints are described in Section 2. As a consistency check, the beam properties at 610 MHz are also inferred from a full-track synthesis in Section 3. The process used to retrieve the

beam response from the holography data is detailed in Section 4, while two-dimensional maps of the full-Stokes beam at 610 MHz are presented in Section 5 along with an analysis of the 325 MHz beam. The obtained beam maps are then applied in order to correct the direction-dependent response. The theory behind these corrections and the impact on wide-field GMRT images is detailed in Section 6. A new technique for EVPA calibration using an interferometer's wide-field response is detailed in Section 7. A discussion of the results is provided in Section 8.

2 Observations

Observations were made with the GMRT, at both 325 MHz and 610 MHz using the software backend. All of the data used in this report are summarised in Table 1.

Table 1: Observations

Date	Obs. Code	Frequency /MHz	Bandwidth /MHz	Integration Time /s
2010 Jan 10	17_052	610	16	16
2011 Apr 26	TST0570	610	16	8
2011 Sep 09	TST0620	325	32	16

Observation 17_052 was a conventional full-track observation of the nearby galaxy M51 in full-polar mode. Standard calibration procedures for GMRT data were used for observation 17_052, with the EVPA calibration applied using 3C286 which is assumed to have a rotation measure (RM) of -1.2 rad m^{-2} and an intrinsic PA of 33° (Garn 2009; Farnes 2012). The observations TST0570 and TST0620 were also flagged and calibrated using similar techniques.

The test observations TST0570 and TST0620 used for analysis of the GMRT full-Stokes beam were taken in modified holography mode. This means that two reference antennas remained fixed on an unpolarised calibrator while the remaining antennas were slewed in azimuth and/or elevation to a co-ordinate such that the calibrator source was observed offset from the phase-centre. In all cases, the two reference antennas were excluded from the data analysis so that only the offset antennas were used – allowing the power pattern[1] to be directly retrieved, rather than the voltage pattern.

A number of offsets were used, such that a grid of 'raster scans' were observed. The grid used for observing these off-axis raster scans is shown in Figure 1. Note that all four axes were only observed at 610 MHz, and the 325 MHz observations excluded the diagonal axes Azimuth-X and Elevation-X.

Each axis of the observing grid included an on-axis scan of the holography source. These on-axis scans were used to solve for the complex gains of each antenna, with the solutions being interpolated across the other raster scans – essentially using the on-axis scans for phase calibration. The effects of instrumental polarisation (and parallactic angle variation at the phase-centre) were removed from the data by solving for the leakages using all on-axis observations of the unpolarised calibrator.

An EVPA calibration was applied to obtain the Q and U beam in the calibrated antenna frame. The correction to the holography data was applied so that the raster scans of the derotated azimuth axis displayed an EVPA that was oriented radially. Evidence to justify this assumption is provided in Section 3.

For the sake of completeness, constraints on the Stokes V beam are obtained in Section 4 but no further attempt is made to correct for this response. Unless otherwise specified, I use the term 'polarised' to refer to linear polarisation throughout this memo.

The sources used for flux and polarisation leakage calibration, along with the unpolarised holography source observed for the off-axis raster scans are summarised in Table 2.

[1]The power pattern is 'superimposed' onto interferometric observations of the sky, and is therefore more fundamental for studying the effect that the beam has on measured source properties.

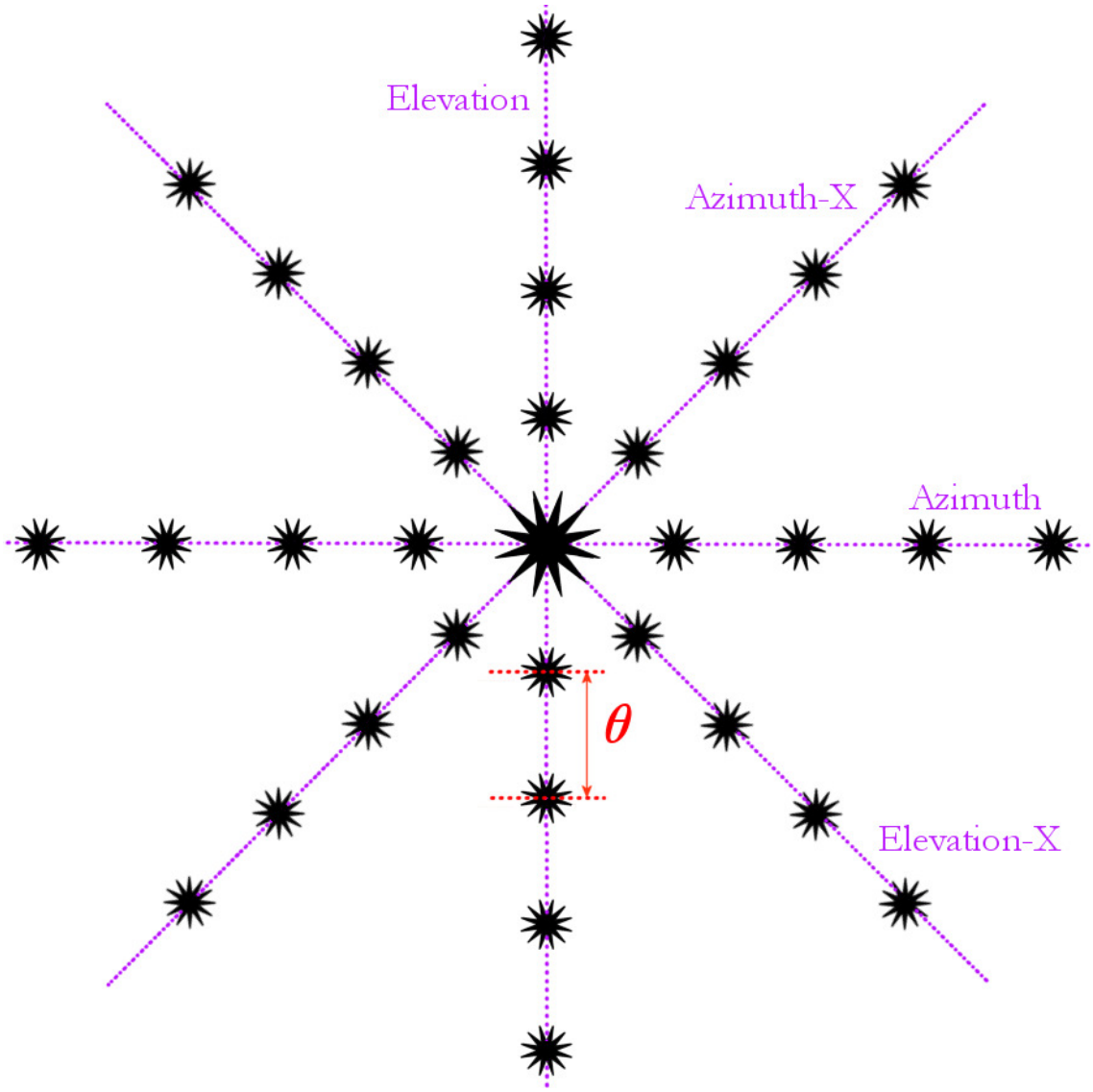

Figure 1: The grid used for observing the off-axis raster scans. Each axis is labelled on the end that I define as positive. Note that the Azimuth-X and Elevation-X axes were only observed at 610 MHz. For the 610 MHz observation, $\theta = 10'$, with 9 raster scans along each axis and a maximum offset of $40'$. The grid for the 325 MHz observation is similar, but uses $\theta = 20'$ to compensate for the larger beam, with a maximum offset of $80'$. The FWHM of the primary beam, as measured at the observatory, is $85.2'$ at 325 MHz and $44.4'$ at 610 MHz.

Table 2: Sources

Obs. Code	Frequency /MHz	Flux & Leakage cal.	Holography source
TST0570	610	3C147	3C147
TST0620	325	3C48 & 3C286	3C48

3 Inferring Direction-Dependent Beam Properties at 610 MHz

A lot can be inferred about the GMRT's off-axis response from a conventional observation. Observation 17_052 has $\sim$ 6 hours on source, with parallactic angle variation ranging from $-86°$ to $+89°$. This observation was used to investigate the effects of direction-dependent instrumental polarisation.

RM Synthesis was performed on the entire FOV surrounding M51, using images that were uncorrected for the Stokes I beam. For a description of RM Synthesis see Brentjens & de Bruyn (2005). For details on the application of RM Synthesis to GMRT data see Farnes (2012).

The Faraday spectrum was processed between ± 2000 rad m^{-2} with sampling every 1 rad m^{-2}. A noise level of 44 μJy beam^{-1} rmsf^{-1} was achieved in the cleaned Faraday cubes (ϕ-cubes). The RMSF has a FWHM of 321 rad m^{-2}. The RMs of the sources in the field were all found to be low. Due to the large FWHM of the RMSF, all of the polarised sources are visible at, or near, a Faraday depth of 0 rad m^{-2}. The wide-field images in Stokes I and in P for a Faraday depth of 0 rad m^{-2} are shown in Figures 2 and 3. Note the lack of instrumental artefacts from residual instrumental polarisation, and the substantial number of discrete polarised sources.

3.1 Polarised Intensity

Sources with peak brightness above a 5σ threshold in Stokes I were manually identified. From the brightest pixel in Stokes I, those sources with a peak brightness $\geq 8\sigma$ in the amplitude of their Faraday spectrum[2] were considered polarised. These sources had their peak brightness in P calculated by fitting a Gaussian to data points surrounding the peak. The calculated peak in P was corrected for the effect of Rician bias using the estimator presented by George et al. (2011). σ was taken from the cleaned Q/U ϕ-cubes. The corrected values were used to calculate the fractional polarisation, $\Pi = P_0/I$. This procedure tends to underestimate the polarisation fraction, as sources may have polarisation structure that is offset from the peak in Stokes I. Nevertheless, the calculated values still provide a good estimate of the polarised intensity resulting from off-axis effects.

Sources with a peak brightness less than 8σ in the Faraday spectrum were considered unpolarised down to the sensitivity limit. The peak in the P image created from band-averaged Q and U was used to place an upper limit on the polarisation fraction of unpolarised sources. This is acceptable as the Faraday depths in the field are small (see Farnes (2012)). Bandwidth depolarisation will only be significant in this

[2]The detection statistics differ in Faraday space. A 7σ detection threshold in ϕ-space has an equivalent false-detection rate to the $\approx 2.5\sigma$ level in total intensity. At 8σ, the false-detection rate is less than 1 in 33,000 (George et al. 2011).

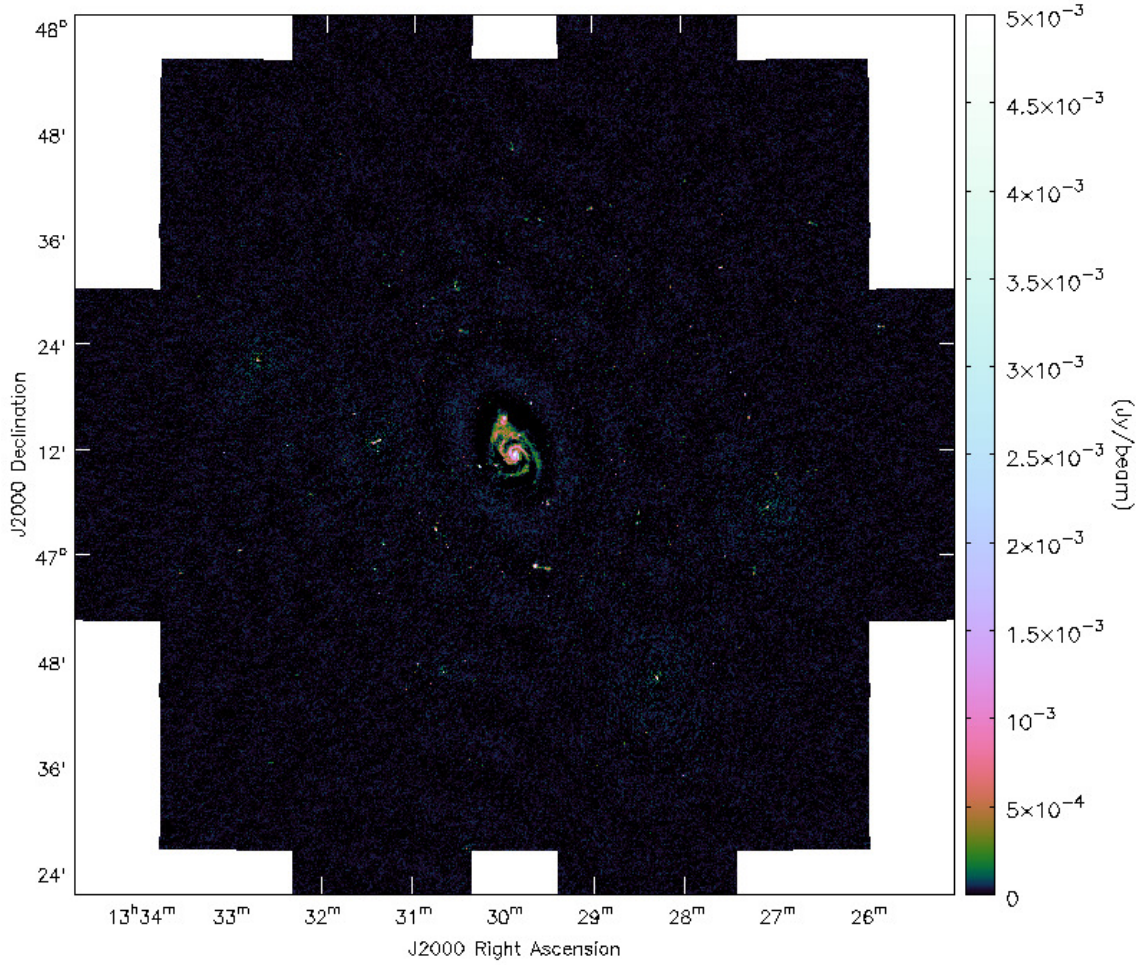

Figure 2: The wide-field Stokes *I* image of the field surrounding M51 at 610 MHz. A correction for the effects of the Stokes *I* beam has not been applied. Also see Figure 3.

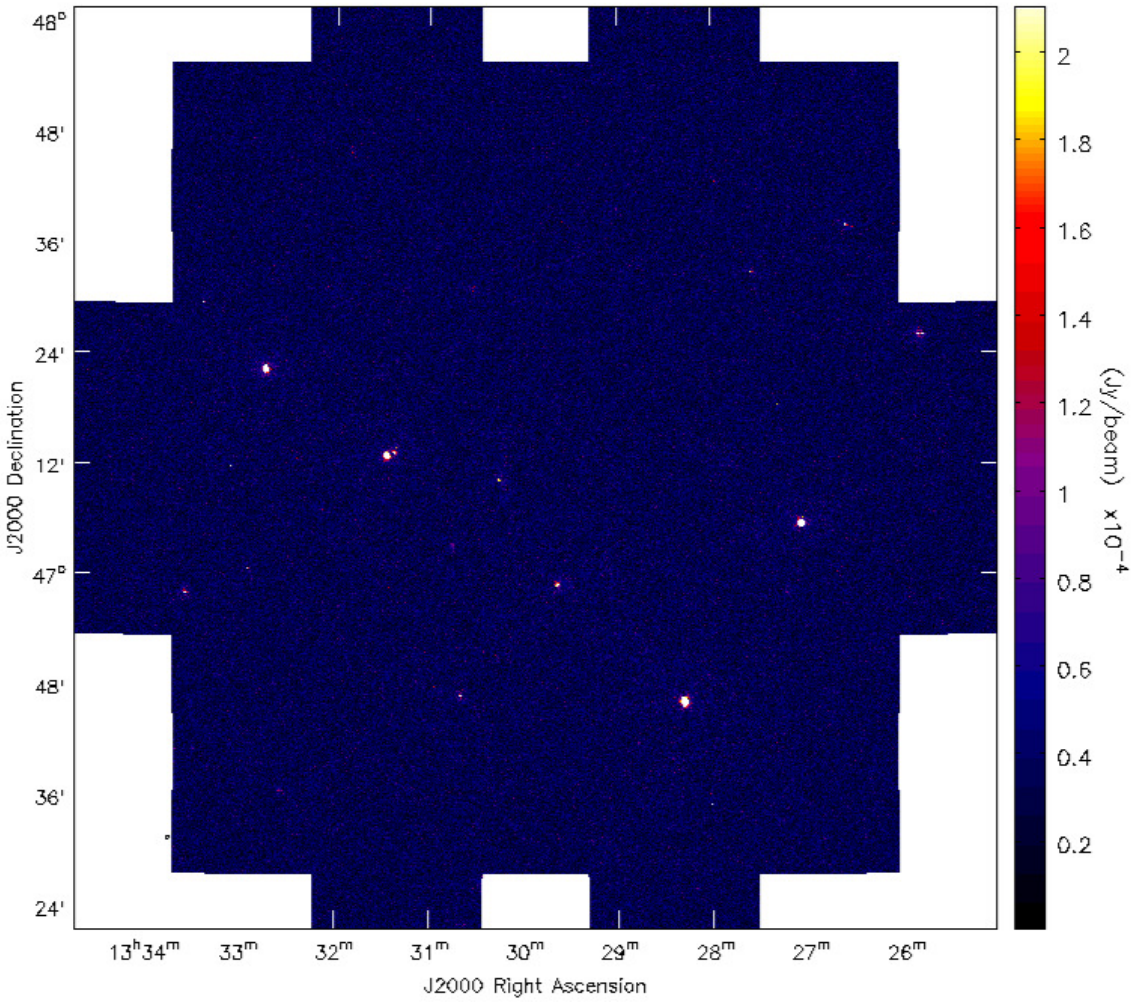

Figure 3: The wide-field image of the field surrounding M51 at 610 MHz in polarised intensity for a Faraday depth of 0 rad m^{-2}. The lack of instrumental artefacts, combined with the large FWHM of the RMSF mean that a Faraday depth of 0 rad m^{-2} is useful for displaying the polarised sources. A correction for the effects of the Stokes *I* beam has not been applied. Also see Figure 2.

field for a RM> 40 rad m^{-2}. The calculated peak was corrected for Rician bias using a Wardle-Kronberg estimator and σ from the Q/U images (Wardle & Kronberg 1974). This procedure tends to overestimate the polarisation fraction, as the bias correction does not work well for low s/n levels (Simmons & Stewart 1985). Nevertheless, the calculated values provide a reasonable upper limit on the polarisation fraction.

A plot of the fractional polarisation of polarised and unpolarised sources as a function of increasing distance from the phase-centre is shown in Figure 4. The plot provides a crude estimate of the direction-dependent instrumental polarisation. It must be remembered that M51 is located near the phase-centre with an angular size covering several arcminutes. The galaxy behaves as a depolarising Faraday screen. If I therefore only consider data beyond 10′, there is no clearly discernible increase in Π out to the half-power point. Between half-power to 10% of the Stokes I beam, the direction-dependent response does appear to steadily increase. The interpretation is hindered by the two polarised sources with $\Pi > 10\%$ in this region of the beam, as it is not clear if these are intrinsically of higher polarisation or are instead affected by beam effects. Beyond the 10% point of the beam, Π increases rapidly.

A direction-dependent response is therefore apparent, with the spurious polarised intensity of sources visibly increasing as a function of distance from the phase-centre. A conservative 'upper limit' on the effect of the polarisation beam at 610 MHz appears to be $\leq 2.5\%$ at the half-power point, with a rapid increase beyond this to $> 20\%$ at the edge of the beam. However, these 'upper limits' truly provide a lower bound. If the polarisation beam is oriented radially, it would be expected that this observation's large range in parallactic angle will have caused the direction-dependent instrumental effects to average down considerably. The 'snapshot' instrumental polarisation is actually best investigated via observation of an off-axis calibrator and is considered in Section 4.

3.2 Frequency-Dependence

It is essential to check the frequency response of the off-axis polarisation. Although different instruments, the WSRT is known to have a frequency-dependent beam pattern with a period of $\sim$ 17 MHz (Farnsworth et al. 2011). The VLA also showed a strong change in off-axis characteristics as a function of IF (Cotton 1994), while the EVLA beam polarisation is essentially frequency-independent across an observing band[3].

The application of RM Synthesis to the field of M51 can also be used to study the frequency-dependence of the direction-dependent polarisation. RM Synthesis is particularly useful as frequency-independent instrumental effects show up at a Faraday depth of 0 rad m^{-2} (Brentjens & de Bruyn 2005). The resulting output at a Faraday depth of 0 rad m^{-2} is shown in Figure 5. The Faraday depths of the sources are low and no additional response was identified at high Faraday depths. This suggests the direction-dependent instrumental polarisation does not change rapidly with frequency.

The frequency-dependence of the beam polarisation can be further examined using bright, spuriously polarised sources located far from the phase-centre. If significant frequency-variation in the beam properties exist, this will manifest as anomalous RMs for sources located off-axis. An NVSS catalogue of source RMs within 1.5 degrees of M51 show that the galaxy is located in an area with a mean RM of 0.06 rad m^{-2},

[3] `http://www.ira.inaf.it/meetings/rm2010/talks/Cotton.pdf`

with σ of $\sim$ 12 rad m^{-2} (Taylor et al. 2009). All sources in the field were found to have consistently low RMs, with no discernible correlation as a function of distance from the phase-centre. The variation in Stokes Q and U for an example source located 30′ off-axis at 13h28m17.9s, 46d46′21″ is shown in Figure 6. The source is clearly visible as the brightest spuriously polarised source to the SW of Figure 2. There is a slight decrease in Stokes Q at the low end of the band as a consequence of the bandpass, but the Q/U response otherwise appears stable with frequency.

In combination with the lack of direction-dependent instrumental polarisation at non-zero Faraday depths, the stable Q/U response as a function of frequency suggests that the wide-field polarisation beam has no significant frequency-dependence across an observing band at 610 MHz.

3.3 Polarisation Vector Orientation

The RM Synthesis performed on the field of M51 can also be used to study the geometry of the direction-dependent polarisation.

The results of RM Synthesis suggest that the off-axis instrumental response is oriented in a predominantly radial manner, as shown in Figure 5. Pen et al. (2009) show that this is anticipated and that leakage across the beam is expected to vary in a quadrupolar pattern. This is due to the GMRT's prime-focus feeds being mounted on four support legs which each have a width comparable to the observing wavelength. Consequently, one expects unpolarised sources within the first null to appear radially polarised, with sources beyond the null being tangentially polarised.

The radial orientation of the polarisation beam is useful for observations obtained during a full-track synthesis, as the radial polarisation will tend to average down over long integrations. This averaging down reduces the direction-dependent response within the half-power points at 610 MHz and assists considerably in reducing spurious polarisation. Nevertheless, I shall show that the snapshot direction-dependent effects are more substantial. The implication is that observations with a science goal requiring wide-field polarimetry should always observe over the full available range in parallactic angle, χ. This can help to reduce direction-dependent effects considerably.

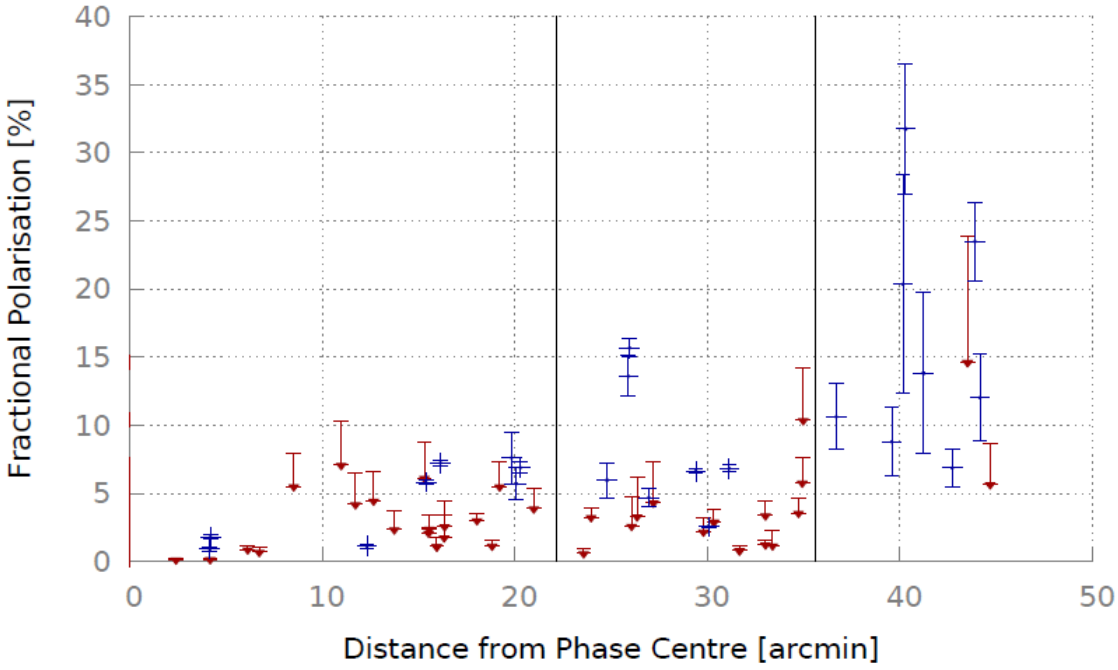

Figure 4: The fractional polarisation, Π, of sources surrounding M51 as a function of distance from the phase-centre. Sources detected above an 8σ limit following RM Synthesis are shown in blue. Sources undetected in polarisation within the sensitivity limit ($P < 8\sigma$) have an upper bound shown in red. The half-power and 10% points of the I beam are indicated by the solid vertical lines.

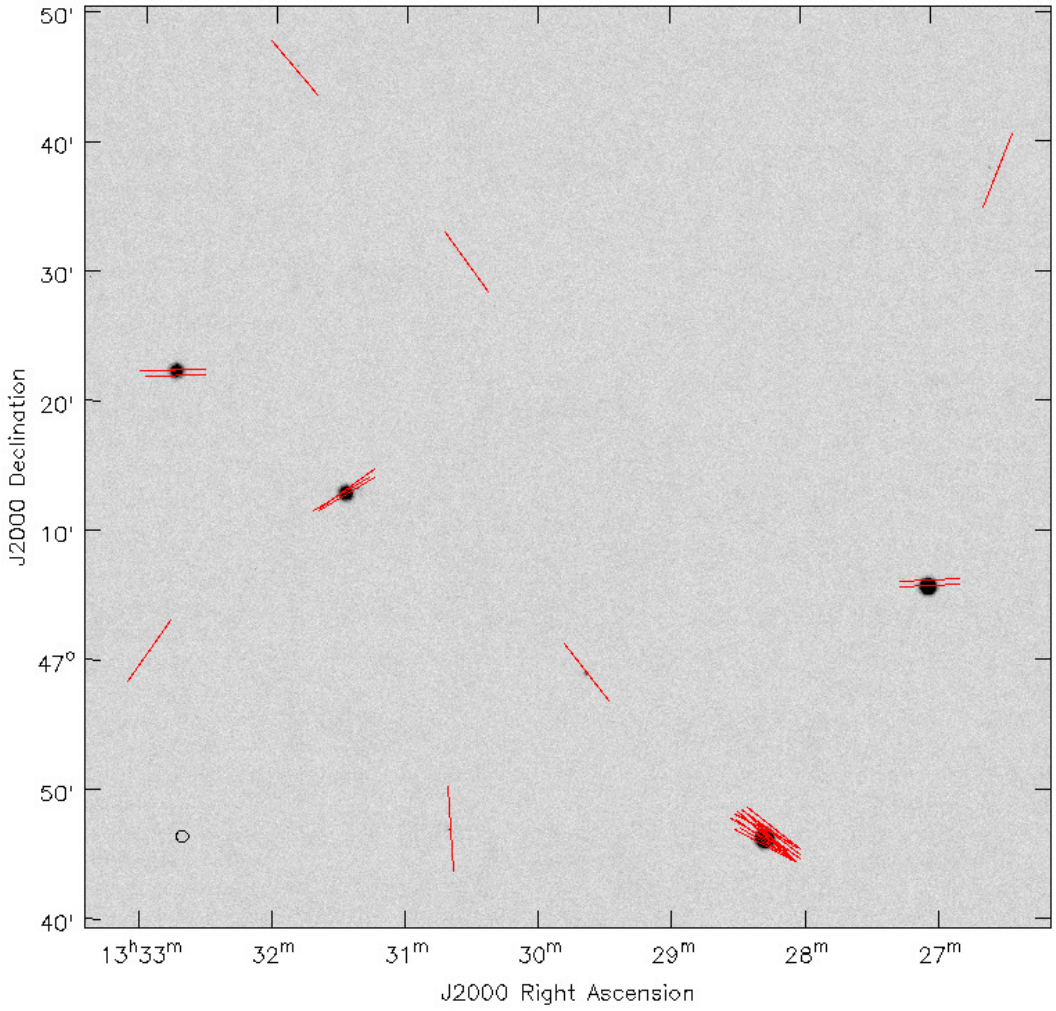

Figure 5: Grayscale image of the bandwidth averaged polarised intensity, $P = \sqrt{Q^2 + U^2}$, of the field surrounding M51 – the image has not been corrected for the Stokes I beam. The centre of the image is also the phase-centre of the observation. Red vectors indicate the orientation of the direction-dependent instrumental polarisation. The vectors are those at a Faraday depth of 0 rad m^{-2}, as obtained via RM Synthesis. The vectors are not proportional to polarised intensity – variations in polarised intensity across the 610 MHz primary beam are shown in Figure 4.

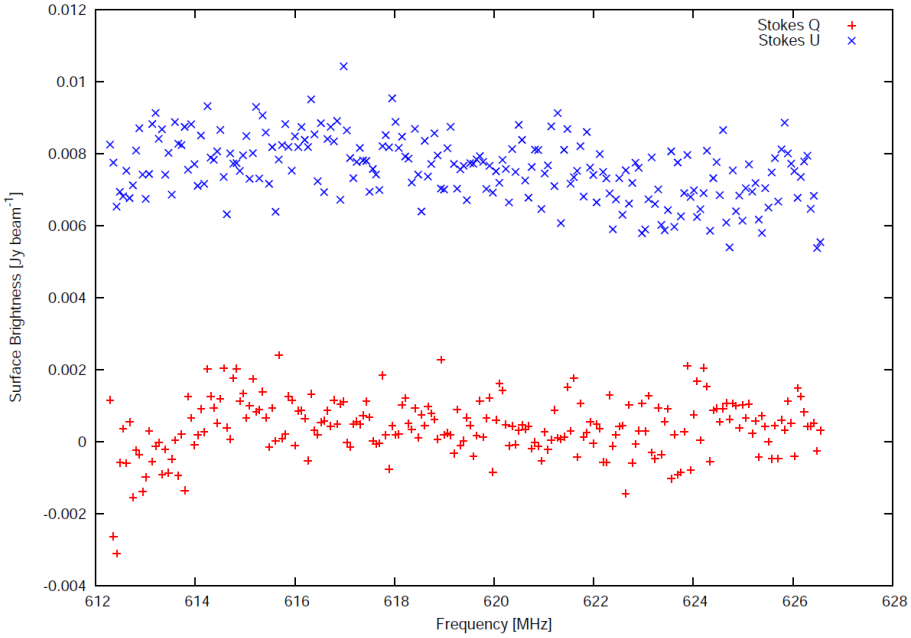

Figure 6: A plot showing the variation in polarised brightness as a function of frequency for a source located 30′ off-axis at 13h28m17.9s, 46d46′21″. Stokes Q and U data are in red and blue respectively.

4 Retrieving the full-Stokes beam from holography rasters

The intention is to measure the direction-dependent instrumental polarisation response so that corrections can be enacted to the *uv*-data. Optimal corrections may ultimately require individual beam models for each antenna, however the computational expense would be highly prohibitive. As such, the effect of the polarisation beam is best represented here by the response of the *average* antenna.

The AIPS task LISTR was used to output the average amplitude and phase of all visibilities, for each holography raster in all four cross-correlations. For an ideal, calibrated interferometer with circular feeds, the cross-correlations are complex quantities defined as:

$$RR = \mathcal{A}(RR)e^{i\psi_{RR}} = I + V \tag{1}$$

$$LL = \mathcal{A}(LL)e^{i\psi_{LL}} = I - V \tag{2}$$

$$RL = \mathcal{A}(RL)e^{i\psi_{RL}} = Q + iU \tag{3}$$

$$LR = \mathcal{A}(LR)e^{i\psi_{LR}} = Q - iU \tag{4}$$

where $\mathcal{A}(jk)$ and ψ_{jk} are the amplitude and phase respectively. For a calibrated point-source, $\psi_{RR} = \psi_{LL} = 0$, so the phase terms of equations 1 and 2 can be neglected. However, the terms ψ_{RL} and ψ_{LR} cause mixing of Q and U and cannot be ignored.

By applying Euler's formula to equations 3 and 4, and then substituting into $RL = LR^*$ yields:

$$\{\mathcal{A}(RL)\cos\psi_{RL} - \mathcal{A}(LR)\cos\psi_{LR}\} + i\{\mathcal{A}(RL)\sin\psi_{RL} + \mathcal{A}(LR)\sin\psi_{LR}\} = 0 \tag{5}$$

which has the solution:

$$\mathcal{A}(RL)\cos\psi_{RL} - \mathcal{A}(LR)\cos\psi_{LR} = 0 \tag{6}$$

$$\mathcal{A}(RL)\sin\psi_{RL} + \mathcal{A}(LR)\sin\psi_{LR} = 0 \tag{7}$$

These solutions can be used to show that for real data, normalised for the effects of the Stokes I primary beam, the fractional polarimetric beam response at a given raster is:

$$\frac{Q}{I} = \frac{\Re(RL + LR)}{RR + LL} \tag{8}$$

$$\frac{U}{I} = \frac{\Im(RL - LR)}{RR + LL} \tag{9}$$

$$\frac{V}{I} = \frac{RR - LL}{RR + LL} \tag{10}$$

while the Stokes I response itself can be obtained from:

$$I = \frac{RR + LL}{2} \tag{11}$$

A code was written in Python and used to calculate the polarisation beam response from the amplitude and phase output by AIPS, in conjunction with equations 8–11. This was done for each holographic raster in each of the individual 220 channels across the

band. All of the holography sources are assumed to be unpolarised at these frequencies, so no correction for source polarisation was required.

The instrumental polarisation and effects of χ-rotation have only been corrected at the phase-centre. These effects are actually direction-dependent and due to the GMRT's alt-az mount, any residual instrumental polarisation will display an EVPA that rotates with χ. All off-axis holographic raster scans had to be corrected for the effects of this χ-dependent mixing of Q and U. This erroneous complication of the earlier on-axis calibration has to be undone by derotating Q and U, so that:

$$(Q' + iU') = (Q + iU)e^{-2i\chi} \tag{12}$$

The derotated Q' and U' can then be used to form a final beam profile in full-Stokes. The obtained beam profiles in full-polarisation across the band are shown at 325 MHz in Figure 7, and at 610 MHz in Figure 8.

The mean response across the band was obtained for each holography raster, so that the beam was described by a single datum per raster – creating a set of nine data per beam axis. Each axis was then fitted with a 5th order polynomial in Stokes I, Q, U, and V using an ordinary least-squares fit. All of the one-dimensional slices through the beam and the corresponding fits are shown at 325 MHz in Figure 9, and at 610 MHz in Figures 10–11. The general shape of each beam slice is well described by the fits.

Beyond the sampling limits of 40′ or 80′ at 610 MHz or 325 MHz respectively, the unconstrained polynomial fits deviate from the likely beam response. This has led to the introduction of artefacts in the beam maps at radii further away from the phase-centre than the sampling limit.

4.1 FWHM of the Stokes I beam

Following polynomial fitting, the FWHM of the Stokes I beam axes at 610 MHz were found to be (46.5′ ± 0.8′), (50.0′ ± 0.9′), (46.5′ ± 0.8′), and (49.8′ ± 0.8′) in Azimuth, Azimuth-X, Elevation, and Elevation-X respectively. This suggests the main lobe of the Stokes I beam has a squircle-shaped geometry at 610 MHz, with the FWHM of the beam increasing by ∼ 7.5% along the diagonal axes.

The FWHM of the Stokes I beam at 325 MHz was found to be (92.3′ ± 1.2′) and (93.1′ ± 1.2′) in Azimuth and Elevation respectively.

The measured FWHM of the primary beam differs from the values determined at the observatory of 85.2′ at 325 MHz and 44.4′ at 610 MHz. This is likely a consequence of both the fitting procedure and expected variations in the Stokes I beam – see Section 8 for additional detail.

5 Two-dimensional mapping of the full-Stokes beam

The polynomial fits from Section 4 were used in order to create two-dimensional maps of the GMRT beam at 610 MHz. As the 325 MHz beam was not sampled along the diagonal axes, it was not possible to create a two-dimensional map at this frequency.

The polynomials describe the off-axis response for each Stokes parameter as a function of radius from the phase-centre, and so were used to tangentially interpolate and grid the beam response around the phase-centre at a given radius. This was

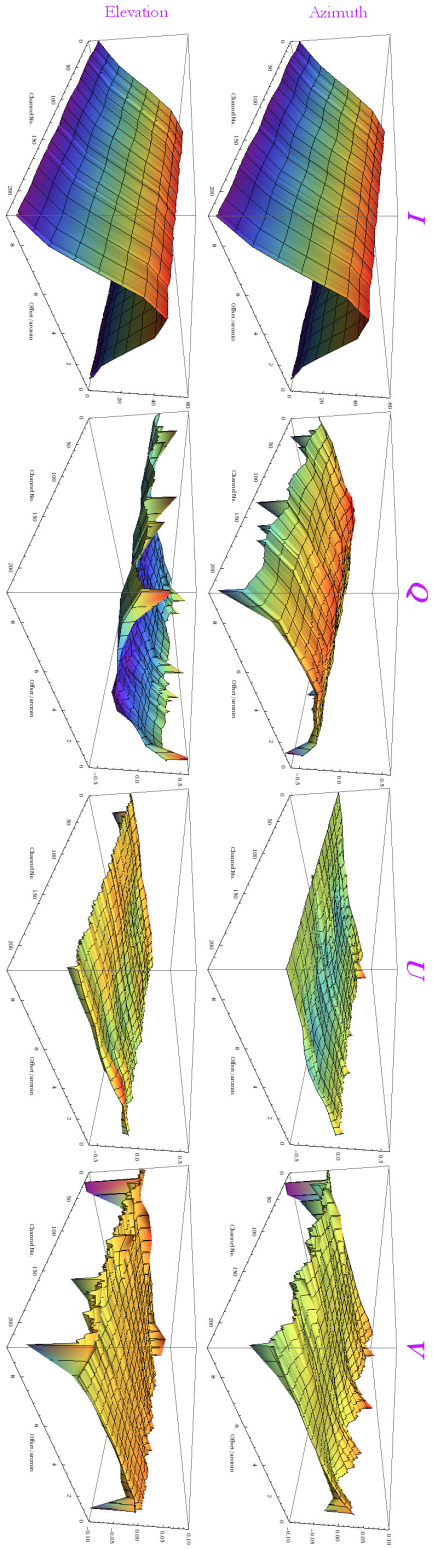

Figure 7: The beam profiles across the band at 325 MHz. The x-axis displays the offset from the phase-centre, the y-axis displays the beam response and is in units of 0–60 Jy for the unnormalised Stokes I beam, and units of fractional polarisation for the other Stokes parameters – the scales range from ±60% for Q and U, and ±10% for V. The z-axis displays the channel number across the band.

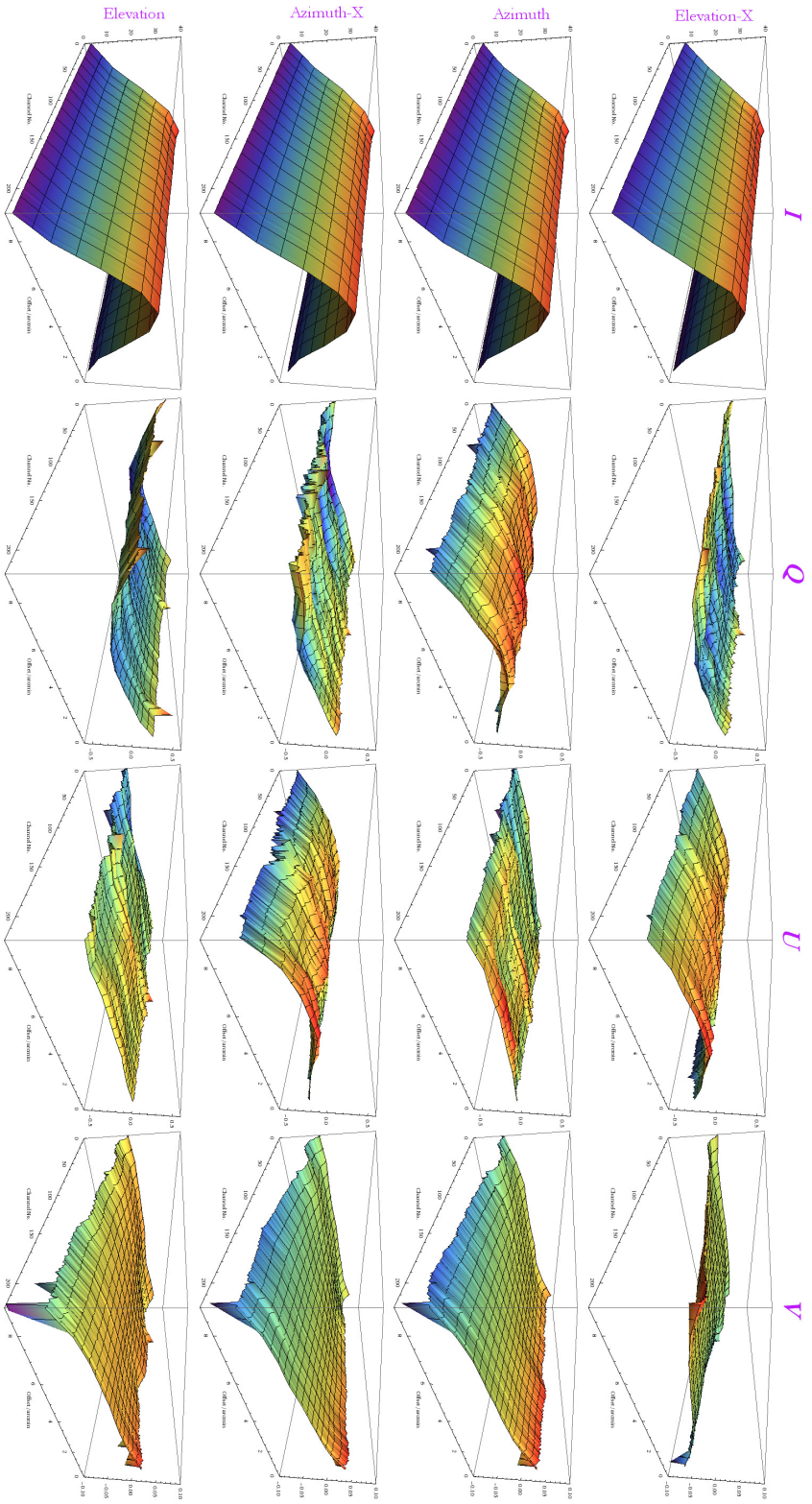

Figure 8: The beam profiles across the band at 610 MHz. The x-axis displays the offset from the phase-centre, the y-axis displays the beam response and is in units of 0–40 Jy for the unnormalised Stokes I beam, and units of fractional polarisation for the other Stokes parameters – the scales range from ±60% for Q and U, and ±10% for V. The z-axis displays the channel number across the band.

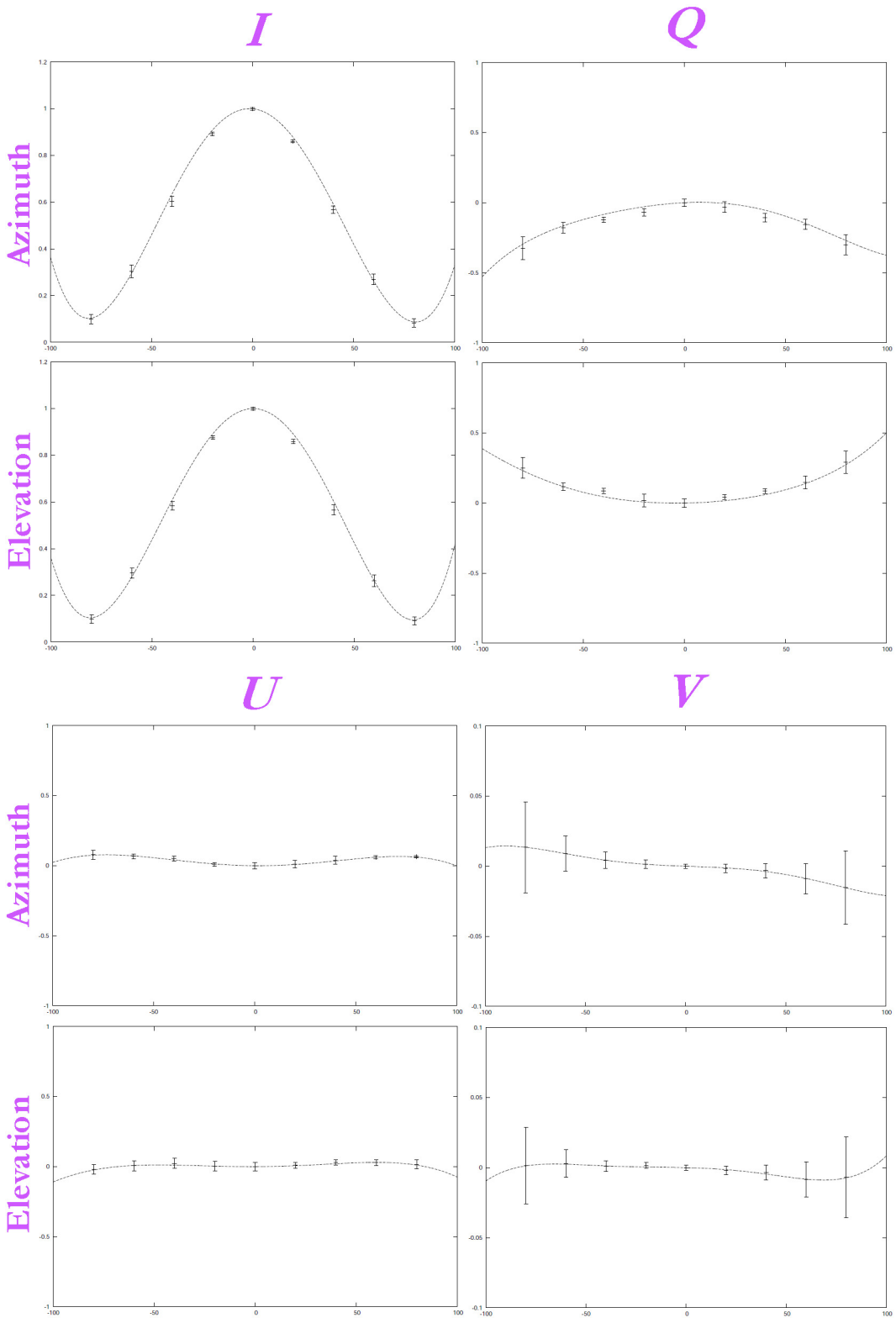

Figure 9: The 5th order polynomial fits to both beam axes for all Stokes parameters at 325 MHz, showing the normalised fractional response as a function of distance from the phase-centre. Stokes I has scales from 0–1.2, Q and U have scales from ±1, and V from ±0.1. Note that the data were sampled out to 80′.

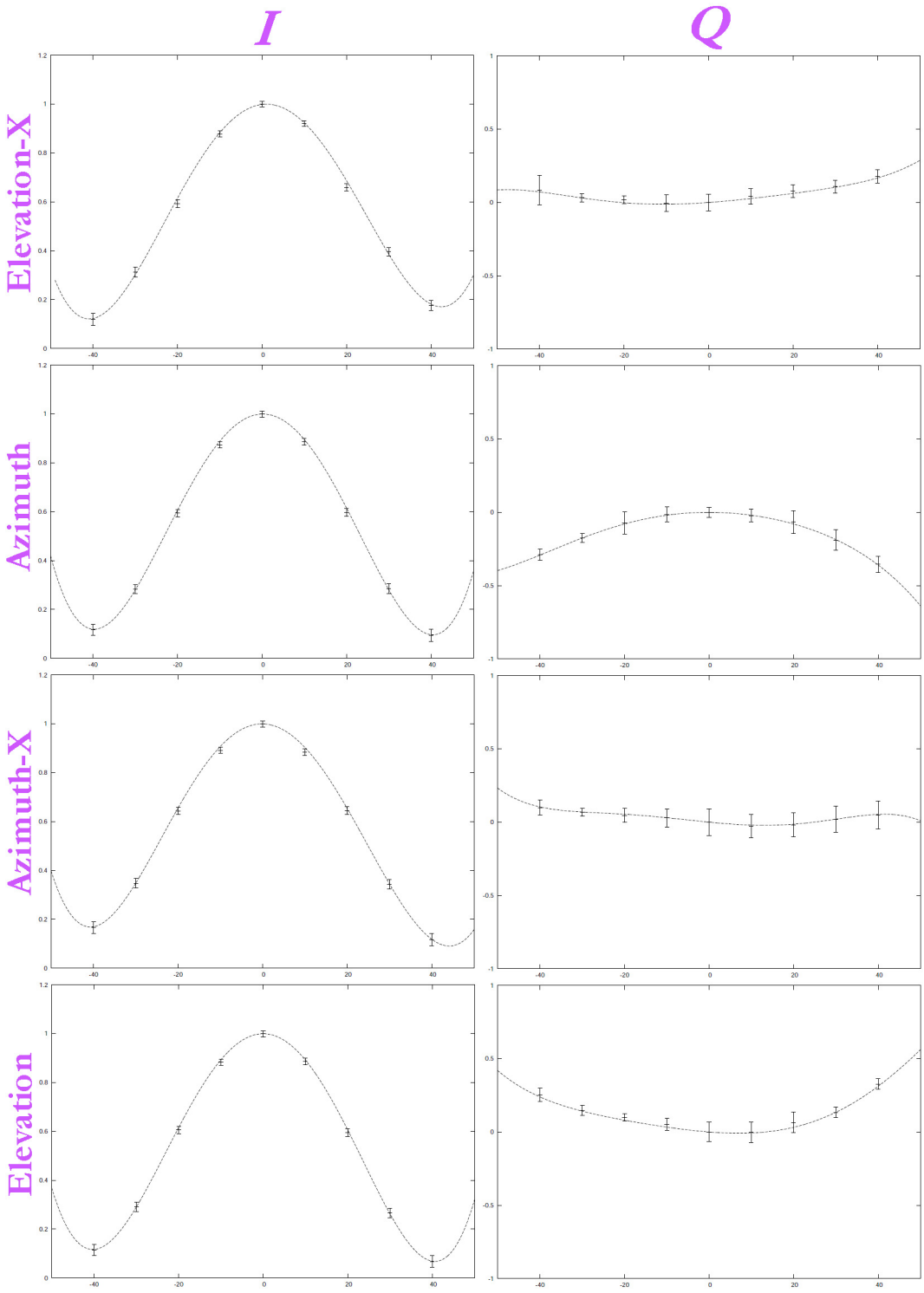

Figure 10: The 5th order polynomial fits to each beam axis for Stokes parameters I and Q at 610 MHz, showing the normalised fractional response as a function of distance from the phase-centre. Stokes I has scales from 0–1.2, while Q has scales from ±1. The fits to U and V are shown in Figure 11. Note that the data were sampled out to 40′.

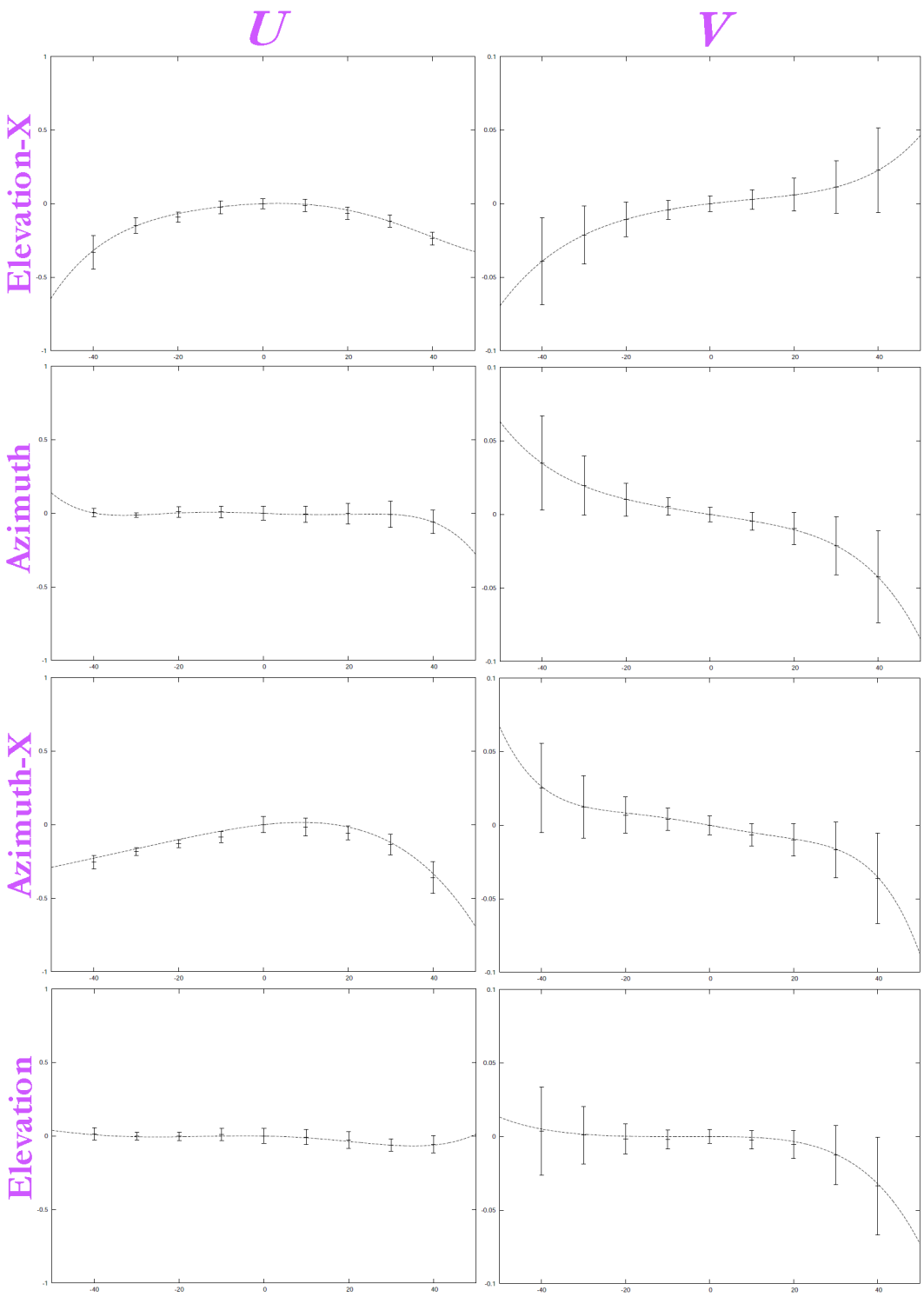

Figure 11: The 5th order polynomial fits to each beam axis for Stokes parameters U and V at 610 MHz, showing the normalised fractional response as a function of distance from the phase-centre. Stokes U has scales from ±1, and V from ±0.1. The fits to I and Q are shown in Figure 10. Note that the data were sampled out to 40′.

carried out using cubic spline interpolation in order to smoothly interpolate the sparsely sampled data over the large tangential distances. Polynomial fitting may have given rise to significant Runge's phenomena.

Further consideration of the 610 MHz polarisation beam response along the diagonal axes suggests a significant problem with the Elevation-X axis. The direction-dependent response along this axis, as displayed in Figures 10–11, appears similar to the Azimuth-X axis. Consequently, polarisation vectors along the Elevation-X axis were oriented tangentially about the phase-centre in the initial Q and U maps – in disagreement with the results of RM Synthesis and the expected quadrupolar response of the GMRT polarisation beam, as discussed in Section 3.

Attempts to correct GMRT direction-dependent instrumental polarisation (see Section 6) failed using this initial beam model, with the polarisation of all sources tending to increase. Images made in AIPS of the off-axis holography sources confirmed that the unusual beam response was a result of the observation itself. As a test, the orientation of polarisation vectors along the Elevation-X axis were rotated so that they were forced to be oriented radially – this rotation was equivalent to a change of sign for both Q and U. The resulting maps are consistent with the response of the GMRT inferred using RM Synthesis, and appear to adequately correct direction-dependent effects. No explanation for this anomaly has been found, and it is crucial that this be checked by further observation.

The final two-dimensional beam at 610 MHz, interpolated under the assumption that the polarisation vectors are oriented radially along all axes, is shown in Figures 12–13.

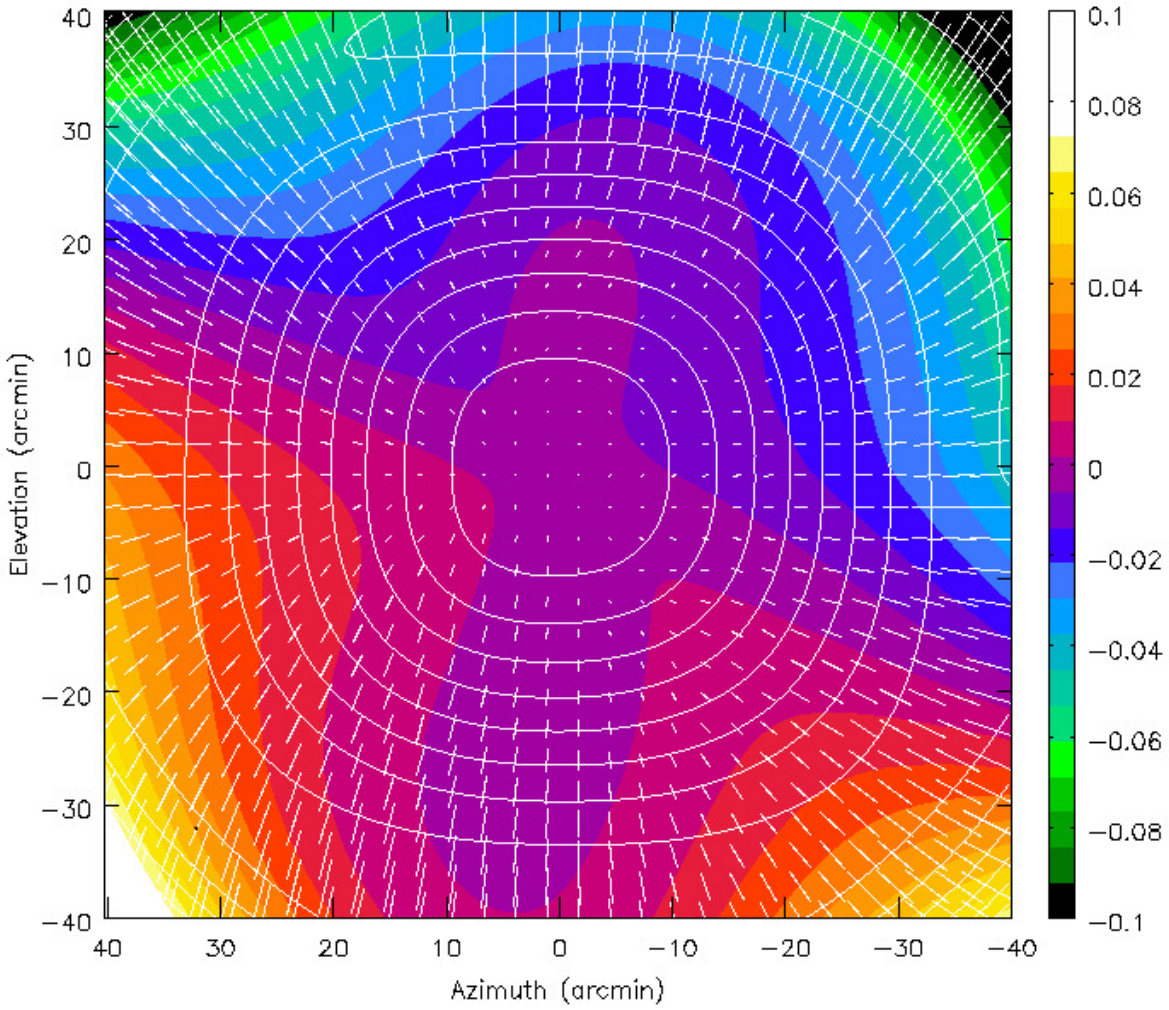

Figure 12: The main lobe of the GMRT primary beam in full-Stokes at 610 MHz. White contours show the Stokes *I* response with contour levels at 10, 20, 30, ..., 90%. White polarisation vectors are proportional to the linearly polarised intensity and indicate the orientation of the linearly polarised response. The Stokes *V* response is shown by the pseudo-colour scale, which ranges from ±10%.

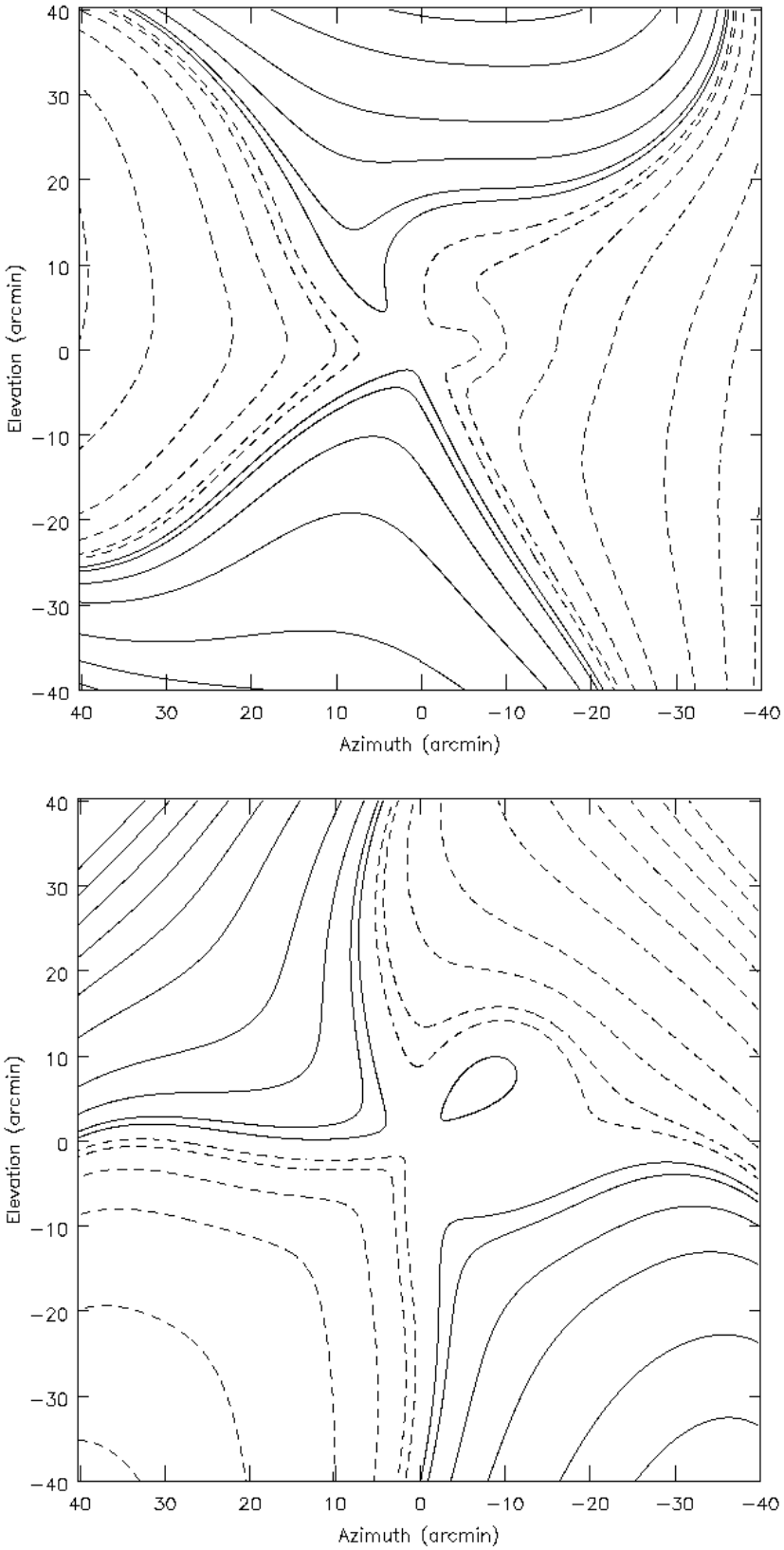

Figure 13: The Stokes Q (top) and U (bottom) fractional instrumental polarisation beam of the main lobe of the GMRT at 610 MHz. Contour levels are at ±1, 2, 5, 10, 20, 30, ..., 70%.

6 Correcting the Wide-field Response

The wide-field response of a radio interferometer is modulated by the full polarisation beam. In order to perform wide-field polarimetry, it is essential to be able to correct for these direction-dependent beam effects. No attempt was made to correct for the effects of spurious circular polarisation.

For linear polarisation observations with alt-az mounted circular feeds, the introduced aberrations are a consequence of three effects. For simplicity, I first consider a 'snapshot' observation, such that the data can be considered as of constant parallactic angle. For this case, polarimetric aberrations are introduced by:

1. The Q and U beam being rotated in the sky-plane by an amount equal to the parallactic angle.
2. Mixing of the Q/U beam response as a consequence of the parallactic angle.
3. The resulting rotated and mixed Q and U fractional polarisation beams allow a fraction of the total intensity to leak into the Q and U images.

For a single snapshot, it is possible to correct for these effects by first rotating the derived Q and U fractional polarisation beams, shown in Figure 13, by χ. The mixing of Q and U is introduced by the on-axis polarisation calibration and the associated correction for parallactic angle variation at the phase-centre – causing any spurious polarisation to rotate in the complex-plane as a function of χ. Similar corrections have previously been applied in the image-plane to VLA data for snapshot observations (Cotton 1994).

As most GMRT polarimetric observations are full-track observations, this procedure is clearly not ideal. As Cotton points out, it is possible to remove direction-dependent effects from full-track observations by independently correcting and imaging each snapshot of constant parallactic angle and averaging the resulting images. However, as CLEAN is a non-linear algorithm, the average of separately imaged 'chunks' of *uv*-data is not identical to a single image of averaged *uv*-data. This limitation has been overcome using a novel technique whereby the clean components from a Stokes I image are scaled by the previously mentioned χ-dependent effects, and the response removed in the *uv*-plane.

Having interpolated the beam model derived in Section 5 to the same geometry as the Stokes I image, the direction-dependent response, $R(x, y, \chi)$, for k clean components is described by:

$$R = \sum_{i=1}^{k} I_i(x,y)\left\{Q(x',y') + iU(x',y')\right\} e^{2i\chi} \ni \begin{bmatrix} x' \\ y' \end{bmatrix} = \begin{bmatrix} \cos\chi & \sin\chi \\ -\sin\chi & \cos\chi \end{bmatrix} \begin{bmatrix} x \\ y \end{bmatrix} \quad (13)$$

where $I_i(x, y)$ is the Stokes I flux of the i-th clean component and $Q(x', y')$ & $U(x', y')$ are the fractional polarisation response obtained from the beam model. The pixel co-ordinates (x, y) and (x', y') are integers as a consequence of pixel quantisation in both the beam model and clean component list positions, and are related through the given rotation matrix. The centre of the map is defined as pixel $(x, y) = (0, 0)$. The mixing of Q and U is analytically identical, but of opposite sign, to that in Equation 12.

The factor of 2 in the exponential originates from degenerate solutions for rotations of $\pm 180n$ degrees.

The response is calculated for each chunk of approximately constant parallactic angle throughout the full-synthesis, and the Fourier Transform of the scaled clean components is then subtracted from the data. The entire *uv*-data is then re-imaged. This method should have the advantage that the associated sidelobes of the spurious instrumental polarisation are also removed from the final images, thereby increasing the dynamic range.

The impact of the corrections on selected off-axis sources is shown in Figures 14–16. The corrections shown here allowed each chunk to have a maximum parallactic angle variation of $\Delta\chi = 10°$.

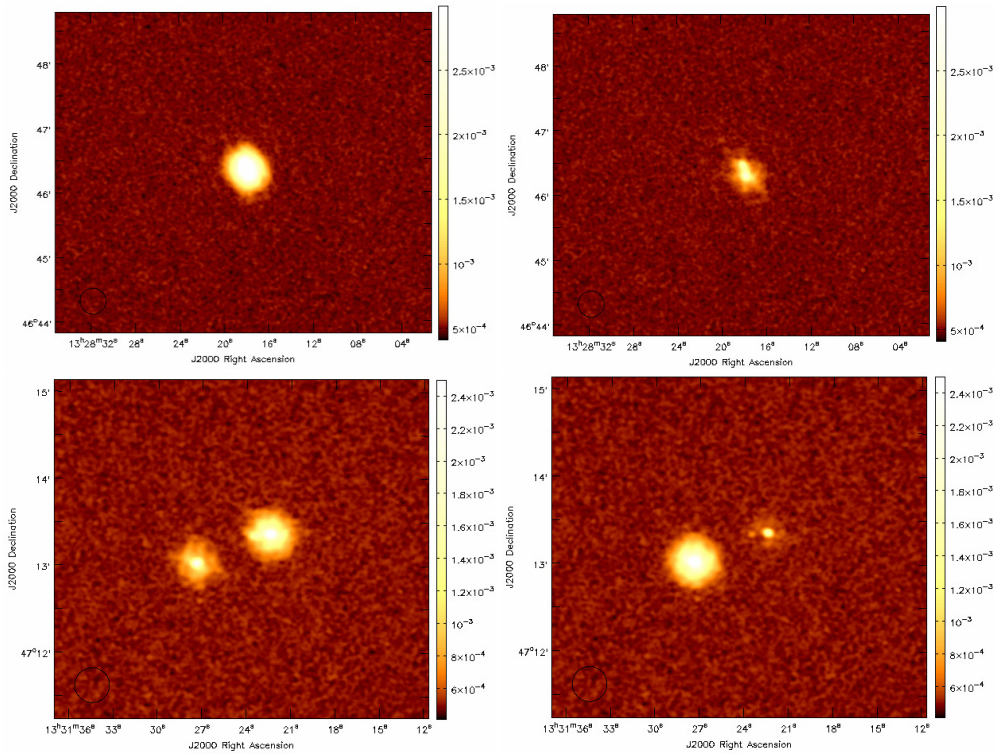

Figure 14: Images of the band-averaged polarised intensity both before (left) and after (right) the corrections for direction-dependent instrumental polarisation effects. Images are shown for two individual sets of sources as displayed to the top and bottom. These sources are located 25.4′ and 15.3′ off-axis respectively. One source (bottom) has its polarised intensity modified in an unusual way (see Section 8). The pseudo-colour scales are in units of Jy beam^{-1}, and the scales are identical for the before and after image of each source.

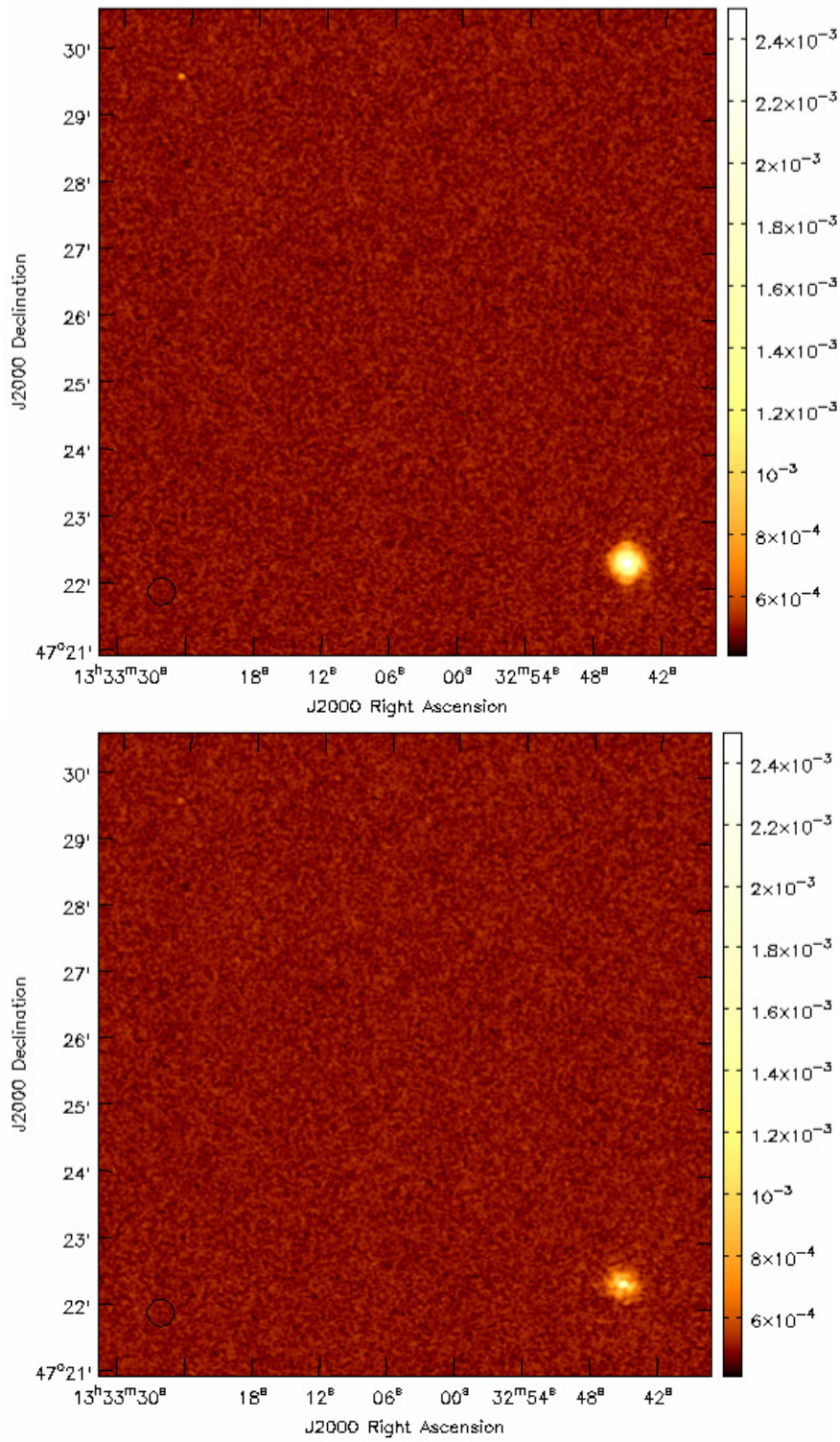

Figure 15: Similar to Figure 14, showing a map of the band-averaged polarised intensity both before (top) and after (bottom) the corrections for direction-dependent instrumental polarisation effects. Two sources – one in the NE and another in the SW – show reduced wide-field effects. The pseudo-colour scales are in units of Jy beam^{-1}, and the scales are identical for the before and after image. The sources are located 14.1′ off-axis.

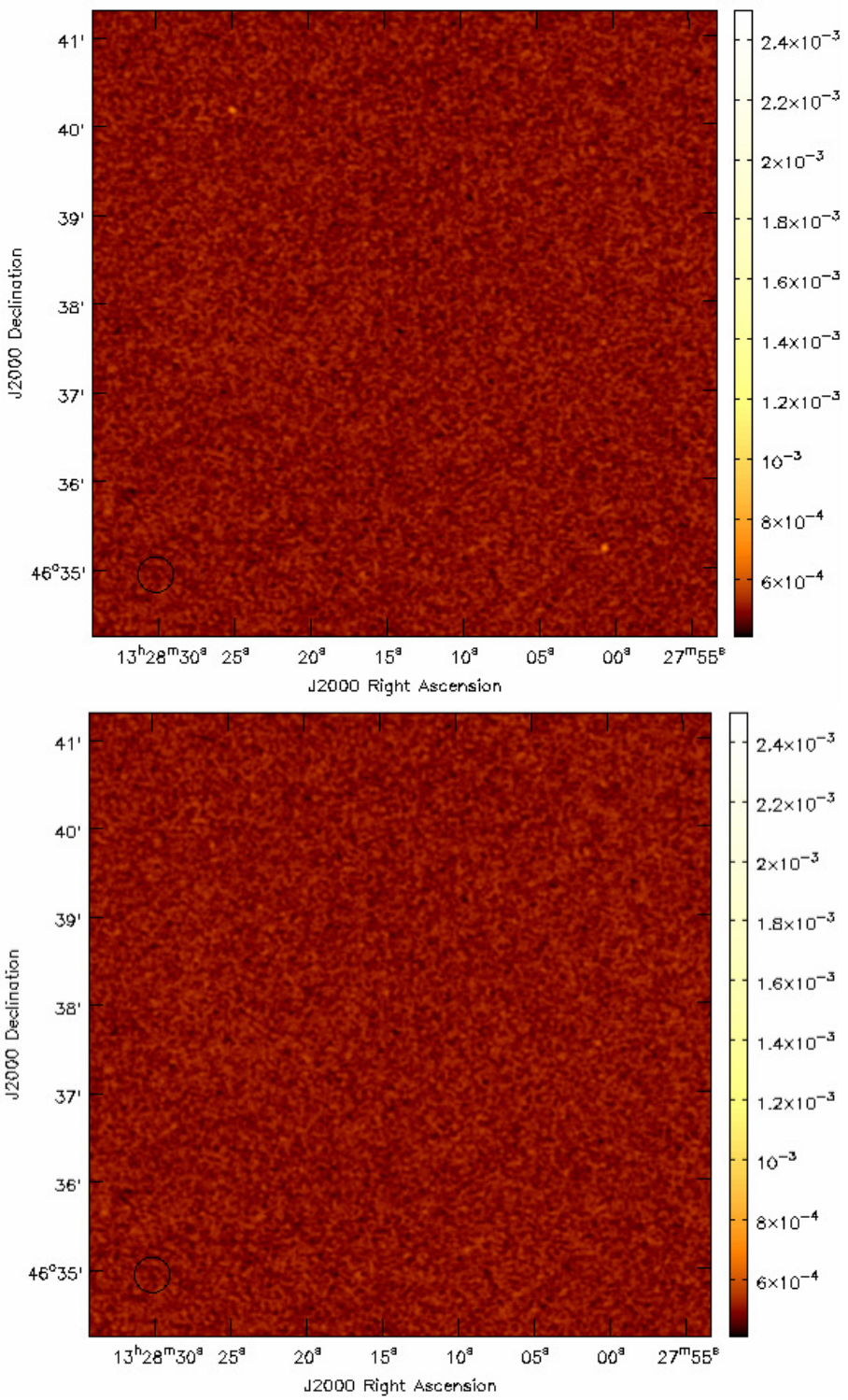

Figure 16: Similar to Figure 14, showing a map of the band-averaged polarised intensity both before (top) and after (bottom) the corrections for direction-dependent instrumental polarisation effects. Two sources – one in the NE and another in the SW – are removed completely from the map. The pseudo-colour scales are in units of Jy beam^{-1}, and the scales are identical for the before and after image. The sources are located 34.3′ off-axis.

7 A New Technique for EVPA Calibration

After solving for the instrumental leakage during polarisation calibration, the absolute value of the phase offset between R and L is left as an unconstrained degree of freedom. This needs to be corrected by observing a source with a known EVPA. The calibrators 3C138 and 3C286 are generally used for this purpose, with the RM and intrinsic EVPA measured at high frequency being used for interpolation to lower frequencies. This limits the quality of EVPA calibration, with errors in these *a priori* values cascading into measurements of RM from a target source. Furthermore, no source on the sky has had it's RM directly measured using circular feeds; as is typical of interferometry, all RM measurements with circular feeds are *relative* to pre-determined values for an EVPA calibrator source.

This is particularly problematic for wide-band spectropolarimetry, as the assumed EVPA and RM of a calibrator source will be used to calibrate the source of interest. Consider an EVPA calibrator that is naively assumed to be well described by a single RM, but actually consists of multiple components at different Faraday depths. The single RM is then used to calibrate an observation of a target source, which is actually fundamentally described by a single RM. The flawed assumptions made about the EVPA calibrator will propagate into the target field, and RM Synthesis of the 'calibrated' target will erroneously yield multiple Faraday components along the line of sight.

Furthermore, ionospheric variations and source variability also have an impact on the current techniques used for EVPA calibration. As depolarisation is significant at low frequencies, there are substantial limitations to the number of sources with both a known, and a stable, intrinsic EVPA and RM. Overcoming this currently involves active searches for sources with 'low variability' – although these calibrator sources are rarely frequently monitored. Even in cases where the calibrators are monitored for variability, the variation is again only determined relative to yet another EVPA calibrator. It is clear that ideally, calibration would be improved if we could manufacture a polarised source in the sky with extremely well-defined and stable properties.

Having a suitable model of the wide-field response of an interferometer allows for EVPA calibration to be applied using the spurious off-axis polarisation of any bright unpolarised source. As the calibrator's 'polarisation' is a consequence of the antenna, such a correction process is independent of ionospheric variation. The process removes the need for calibration relative to any reference source, and instead makes the calibration relative only to the interferometer's beam.

In the case of the GMRT, the beam model has shown the wide-field response to be both frequency-independent and oriented radially. In order to correct the data, the off-axis mixing of Q/U as described in Equation 12 has to be taken into account. Hence the correction to be enacted in the AIPS task CLCOR is given by:

$$\text{CLCORPRM}(1) = 2\chi - 180 - \psi_{RL} \tag{14}$$

where χ is the parallactic angle of the off-axis scan of the unpolarised source, and $\psi_{RL} = \psi_{LR^*}$ is the RL-phase as either output by task RLDIF or determined from the integrated Q and U flux in the images such that:

$$\psi_{RL} = 2\phi = \arctan\left(\frac{\Sigma U}{\Sigma Q}\right) \tag{15}$$

Taking Equation 12 and substituting in $Q = p_0 \cos 2\phi$ and $U = p_0 \sin 2\phi$ yields:

$$(Q' + iU') = p_0 \{\cos(2\phi - 2\chi) + i \sin(2\phi - 2\chi)\} \tag{16}$$

and so following calibration the measured EVPA of the off-axis source is given by ϕ, while the EVPA of the source in the antenna frame (i.e. independent of parallactic angle effects), ϕ', is given by:

$$\phi' = \phi - \chi \tag{17}$$

This method was tested at the GMRT, with knowledge of the full-Stokes beam used to correct the EVPA using 3C48 at 325 MHz. The calibrated data were used to determine the RM of B1937+21. The corrections yield a RM=+8.2 ± 0.4 rad m^{-2} for B1937+21 at 325 MHz – in excellent agreement with the previously determined value at this frequency of +8.5 ± 0.5 rad m^{-2} (Brentjens 2008). The variations in the EVPA as a function of λ^2 is shown for B1937+21 at 325 MHz in Figure 17.

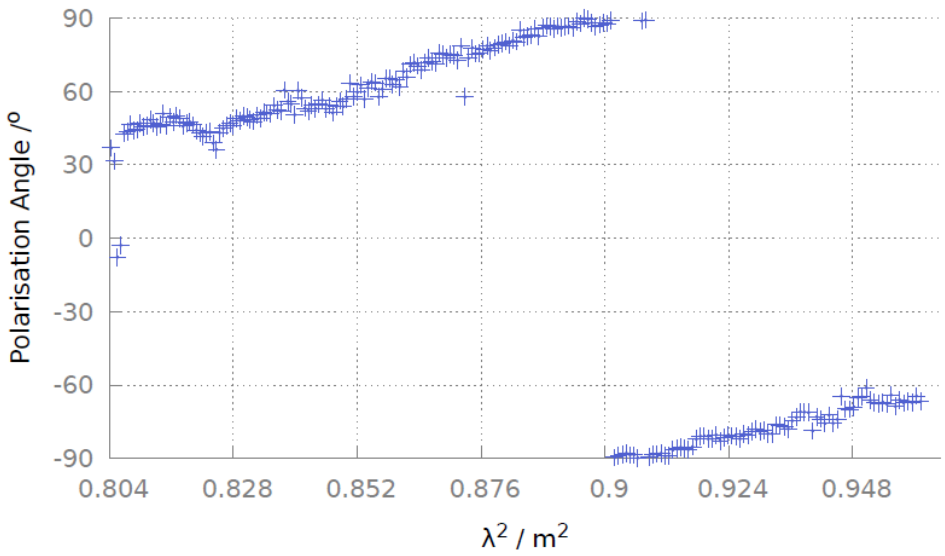

Figure 17: A plot of the EVPA as a function of λ^2 for B1937+21 at 325 MHz, following EVPA calibration using the direction-dependent response of the GMRT.

Using the direction-dependent response of an interferometer to calibrate the EVPA may be particularly useful for facilities such as LOFAR and the MWA – where the science requires highly accurate determination of source RMs, with ionospheric effects eliminated from the data. The corrections are limited only by knowledge of the beam model. The caveat is that the interferometer that is being calibrated must have significant direction-dependent instrumental polarisation.

8 Discussion

A classical model of beam squint/squash in prime-focus feeds suggests that beam squash can arise in Q/U due to two effects: the interaction of the linearly polarised vectors with the curvature of the reflecting surface, and the difference between the two polarisations

in illumination of the primary surface (which occurs from pseudo-waveguide modes in a feed). Similarly, beam squint should arise in V due to the feed not pointing directly at the vertex of the paraboloid. There is no anticipation of beam squint in Q/U or beam squash in V (Heiles et al. 2003).

The fundamental cause of direction-dependent instrumental linear polarisation is the curved reflecting surface, which slightly changes the direction of an incident electric vector upon reflection. For on-axis sources, these polarimetric aberrations cancel out. For off-axis sources, the path length to the source from different parts of the reflecting surface are not all equal. These distortions increase with curvature (Heiles 2002; Tinbergen 1996). Reassuringly, the instantaneous Q/U beams deduced at 325 MHz and 610 MHz are compatible with this model, as the direction-dependent effects appear to scale with the FWHM of the Stokes I beam – implying that the beam squash is a result of interaction with the curved reflecting mesh, and not a consequence of the feed itself.

The constraints placed on direction-dependent effects across the GMRT beam show that the snapshot 610 MHz instrumental response increases to $\sim 10\%$ at the half-power point, and increases rapidly to $> 30\%$ beyond 10% of the Stokes I beam. The measured beam squash suggests that mosaicing snapshot observations would not be sufficient to overcome off-axis effects at the GMRT, as the half-power point snapshot P of $\sim 10\%$ at 610 MHz is greater than the expected median source polarisation of $\sim 2.5\%$ at this frequency. Nevertheless, the full-track observation of M51 shows that this instantaneous instrumental polarisation can average down substantially over a large range in parallactic angle. The 325 MHz snapshot instrumental polarisation is similar to that at 610 MHz, and increases to $\sim 10\%$ at the half-power point, and to $\sim 30\%$ at 10% of the Stokes I primary beam.

Consequently, full-track observations should be used to reduce direction-dependent effects at the GMRT. The use of mosaicing would reduce these off-axis effects further by an additional factor of ~ 2. As a conservative upper limit for observations taken over a large χ-track, the instrumental polarisation at 610 MHz is at most $\sim 2.5\%$ at the half-power point, increasing steadily to $> 20\%$ beyond 10% of the Stokes I beam. Previous analyses of the 150 MHz GMRT beam are also possibly consistent with the off-axis response averaging down as a function of χ, with an instrumental polarisation of $\sim 2.5\%$ at the half-power point for a full-track observation (Pen et al. 2009). However, no measurements of the instantaneous 150 MHz beam are currently available. Given the previously discussed scaling of direction-dependent effects with frequency, it is likely that the 150 MHz instantaneous beam is also simply a scaled version of the 610 MHz beam model shown in Figure 12.

Although not derived here, this scaling with frequency should in principle allow for the beam to be parameterised by a single mathematical function across all observing bands. This leads to the possibility that the GMRT Stokes I beam can also be defined by a single model for all frequencies, similar to the $\cos^6(c \times n \times r)$ derived for the WSRT (Popping & Braun 2008). Variations in the Stokes I beam-width at the GMRT are expected, and the FWHM at 610 MHz is known to range from $42.3'$–$47.2'$ in elevation, and from $42.3'$–$47.0'$ in azimuth (Nimisha Kantharia: priv. comm.). However, the beam results suggest that the 610 MHz primary beam has a squircle-like geometry, with the FWHM increased by $\sim 7.5\%$ along the diagonal axes – coincident with the location of the feed support legs. Peeling is often required at the GMRT at this frequency, and may be a result of time-variable direction-dependent gains caused by the Stokes I beam

rotating on the sky with varying χ. It would be interesting to employ more refined beam models in *a*-projection algorithms, which are able to remove such effects (Bhatnagar et al. 2008).

The classical model of beam squint suggests that for observations of circular polarisation with a parabolic reflector and a feed perfectly aligned with the vertex of the paraboloid, there is perfect circular symmetry and therefore no beam structure in V. However, if the feed deviates slightly from the vertex along the x-direction, then the two circularly polarised beams will point in slightly different directions along the y-direction (Heiles 2002). This suggests that spurious V emission could be more significant in azimuth at the GMRT, as the rotating feed turret (which rotates about the elevation axis) may not lock exactly into place and point directly towards the vertex of the dish. Indeed, the Stokes V beam measured here is increased marginally in azimuth compared to elevation, by a magnitude of $\sim 1.5\%$. It is likely the Stokes V beam therefore changes with each rotation of the feed turret.

The results from RM Synthesis at 610 MHz are consistent with the instrumental linear polarisation being oriented radially with respect to the phase-centre. The analyses of the beam, at both 325 MHz and 610 MHz, are also largely consistent with a radial orientation, with the notable exception of data from the Elevation-X axis at 610 MHz. This anomaly could feasibly be a result of gravitational deformation of the feed support legs, however why this should only afflict one axis is unclear. Nevertheless, such flips in the beam are not unprecedented. Although a very different instrument, the Green Bank Telescope (GBT) has a polarisation beam that flops by 90° randomly, which is equivalent to a change in sign (Heiles et al. 2003). This is analogous to the flip observed at the GMRT. The flip along the Elevation-X axis may therefore indicate that the beam is not constant at different epochs. If this is the case at the GMRT, this will inhibit wide-field polarimetric observations as an unfeasible amount of preparatory time will be required to monitor a possibly unstable beam response. It could also be that blockage from the feed support legs lead to a localised change in the EVPA directly along the Elevation-X axis – if this is the case, the beam must exhibit rapidly varying properties near to the diagonal axes. The lack of a flip along the Azimuth-X axis (which would also be subject to blockage from the feed supports) is contrary to this. Ultimately, all of these possibilities amount to speculation as there is insufficient evidence to firmly conclude the nature of the beam flip – an unknown error during data collection cannot be ruled out. It is important to re-observe the beam and provide more constraints. Nevertheless, rotation of the Elevation-X axis so that it is oriented radially allows for direction-dependent effects to be removed successfully from *uv*-data.

The polarisation beam corrections implemented in Section 6 are novel in that they directly correct the *uv*-data using a Stokes I model of an observed field. These corrections have been used to successfully correct for direction-dependent instrumental polarisation – although by far less than had been hoped and with a number of limitations. The spurious linear polarisation is typically reduced by a factor of $\sim$2. Although useful, the beam corrections work best at correcting instrumental effects beyond the half-power point. The computational expense is therefore unlikely to be worthwhile, particularly when an equivalent or better reduction of the instrumental effects could be achieved via the combination of large parallactic angle ranges and mosaicing. Nevertheless, the corrections could be improved by implementing a cut-off for the Stokes I clean components, as noise and low-level artefacts that are cleaned in Stokes I currently get

added into the linear polarisation images. Additionally some sources increase in P as shown in Figure 14. This can be expected depending on the precise combination of source and instrumental polarisation, but may also suggest that the beam model is not sufficiently accurate. The latter is likely as the direction-dependent corrections implemented here reduce the instrumental polarisation most effectively at distances $> 30'$ from the phase-centre i.e. where the corrections are of a larger magnitude. Limitations to the corrections may result from the decrease in signal-to-noise of rasters near to the phase-centre, significant beam variation between individual antennas, the coarse sampling used, or because of assumptions of χ constancy in each snapshot. In the corrections presented in this report, each chunk has $\Delta\chi < 10^{\circ}$, and no attempt to test the effects of different $\Delta\chi$ has been made. Nevertheless, reasonable wide-field polarimetry is possible at the GMRT via the use of full χ-tracks. Such direction-dependent corrections will be most useful in efforts to retrieve the intrinsic EVPA of sources, which is clearly corrupted by the instrumental beam – as shown in Figure 5.

New data are needed to improve the beam model and consequently the corrections. An attempt to monitor the beam out to the first sidelobe, with more axes, and less sparsely-sampled rasters would significantly enhance the model. The recommendation would be that tests are performed, the feed turret rotated, and the tests repeated in order to rule out epoch-dependent variations due to locking of the feed turret mechanism. This would also allow for checks on the observed change in sign along the Elevation-X axis. Such observations, if taken for all GMRT bands, may provide the possibility of describing the beam with a unified model which is a function of frequency.

Knowledge of a telescope's beam is extremely important, as demonstrated by the ability to calibrate the EVPA using the direction-dependent response – allowing for corrections that are independent of ionospheric effects. Improving the beam model at the GMRT is one of the most important endeavours that could currently be carried out to refine the instrumental response, and follow-up observations should be strongly considered. Such observations may lead to improvements in the pointing model and dynamic range at all frequencies.

References

Bhatnagar S., Cornwell T. J., Golap K., Uson J. M., 2008, A&A, 487, 419.
Brentjens M. A., 2008, A&A, 489, 69.
Brentjens M. A., de Bruyn A. G., 2005, A&A, 441, 1217.
Cotton W. D., AIPS Memo #86, "Widefield Polarisation Correction of VLA Snapshot Images at 1.4 GHz", 1994.
Heiles C., Arecibo Observatory Technical Memo AOTM 99-02, "The LBW Feed: Pointing Accuracy, Beamwidth, Beam Squint, Beam Squash', 1999.
Heiles C., "Single-Dish Radio Astronomy: Techniques and Applications", ASP Conference Proceedings, 278, 2002.
Heiles C., Robishaw T., Troland T., Anish Roshi D., "GBT Commissioning Memo #23", 2003.
Farnes J. S., "Polarimetric Observations at Low Radio Frequencies", PhD thesis, University of Cambridge, 2012.
Farnsworth D., Rudnick L., Brown S., 2011, AJ, 141, 191.
Garn T. S., "610 MHz observations of galaxy evolution", PhD thesis, University of Cambridge, 2009.
George S. J., Stil J. M., Keller B. W., 2011, arXiv 1106.5362.
Pen U.-L., Chang T.-C., Hirata C. M., Peterson J. B., Roy J., Gupta Y., Odegova J., Sigurdson K., 2009, MNRAS, 399, 181.
Popping A., Braun R., 2008, A&A, 479, 903.
Simmons J. F. L., Stewart B. G., 1985, A&A, 142, 100.
Taylor A. R., Stil J. M., Sunstrum C., 2009, ApJ, 702, 1230.
Tinbergen J., "Astronomical Polarimetry", Cambridge University Press, 1996.
Wardle J. F. C., Kronberg P. P., 1974, ApJ, 194, 249.

Acknowledgements

I am exceptionally grateful to Nimisha Kantharia, who has spent extensive time obtaining the high-quality test observations used within this report, and also to Anna Scaife and Russ Taylor for many insightful conversations and useful comments on the manuscript.